Journal of Power Sources 326 (2016) 459–465

Contents lists available at ScienceDirect

Journal of Power Sources

journal homepage: www.elsevier.com/locate/jpowsour

An efficient electrocatalyst as cathode material for solid oxide fuel cells: $BaFe_{0.95}Sn_{0.05}O_{3-\delta}$

Feifei Dong [a, *], Meng Ni [a], Wei He [a], Yubo Chen [b], Guangming Yang [b], Dengjie Chen [c], Zongping Shao [b]

[a] Building Energy Research Group, Department of Building and Real Estate, The Hong Kong Polytechnic University, Hung Hom, Kowloon, 999077, Hong Kong, China
[b] State Key Laboratory of Materials-Oriented Chemical Engineering, College of Chemistry & Chemical Engineering, Nanjing Tech University, No. 5 Xin Mofan Road, Nanjing, 210009, China
[c] Department of Chemistry, Jinan University, Guangzhou, 510632, China

HIGHLIGHTS

- $BaFe_{0.95}Sn_{0.05}O_{3-\delta}$ holds a single cubic structure at fuel cell operating temperature.
- High oxygen vacancy concentration and fast oxygen kinetics are observed.
- Testing cells exhibit superior electrocatalytic activity and long-term stability.

GRAPHICAL ABSTRACT

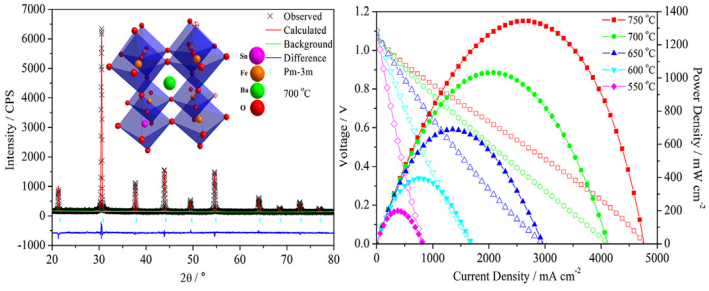

ARTICLE INFO

Article history:
Received 21 May 2016
Received in revised form
2 July 2016
Accepted 7 July 2016

Keywords:
Solid oxide fuel cell
Cathode
Electrocatalyst
Doped-$BaFeO_{3-\delta}$
Tin

ABSTRACT

The B-site substitution with the minor amount of tin in $BaFeO_{3-\delta}$ parent oxide is expected to stabilize a single perovskite lattice structure. In this study, a composition of $BaFe_{0.95}Sn_{0.05}O_{3-\delta}$ (BFS) as a new cathode material for intermediate-temperature solid oxide fuel cells (IT-SOFCs) is synthesized and characterized. Special attention is paid to the exploration of some basic properties including phase structure, oxygen non-stoichiometry, electrical conductivity, oxygen bulk diffusion coefficient, and surface exchange coefficient, which are of significant importance to the electrochemical activity of cathode materials. BFS holds a single cubic perovskite structure over temperature range of cell operation, determined by in-situ X-ray diffraction and scanning transmission electron microscope. A high oxygen vacancy concentration at cell operating temperatures is observed by combining thermo-gravimetric data and iodometric titration result. Furthermore, electrical conductivity relaxation measurement illustrates the fast oxygen bulk diffusion and surface exchange kinetics. Accordingly, testing cells based on BFS cathode material demonstrate the low polarization resistance of 0.033 Ω cm^2 and high peak power density of 1033 mW cm^{-2} at 700 °C, as well as a relatively stable long-term operation for ~300 h. The results obtained suggest that BFS perovskite oxide holds a great promise as an oxygen reduction electrocatalyst for IT-SOFCs.

* Corresponding author.
E-mail address: ff.dong@polyu.edu.hk (F. Dong).

http://dx.doi.org/10.1016/j.jpowsour.2016.07.023
0378-7753/

1. Introduction

Compared to the conventional power generation systems, the high chemical-to-electrical efficiency, flexible fuel sources, and low emissions of solid oxide fuel cells (SOFCs) render them attractive energy conversion technologies in the sustainable energy future [1–3]. However, several barriers including high cost and poor reliability, originating from the high-temperature operation (typically 800–1000 °C), hinder the widespread SOFC commercialization. Lowering the operating temperature to an intermediate range (500–800 °C) can help lower the cost and improve the stability of SOFC but its electrochemical performance is also decreased partly due to the decreased activity of cathode materials for oxygen reduction reaction (ORR) [4,5]. Therefore, creation of robust cathode materials with high electrocatalytic activity for ORR is essential for the development of commercially-viable SOFCs. To date, extensive efforts have been devoted to developing new materials for oxygen electrocatalysis, such as $La_{1-x}Sr_xMnO_{3-\delta}$ (LSM) [6,7], $Sm_{0.5}Sr_{0.5}CoO_{3-\delta}$ (SSC) [8,9], $La_{1-x}Sr_xCo_{1-y}Fe_yO_{3-\delta}$ (LSCF) [10,11], $Ba_{0.5}Sr_{0.5}Co_{0.8}Fe_{0.2}O_{3-\delta}$ (BSCF) [12,13], $LaNi_{1-x}Fe_xO_{3-\delta}$ (LNF) [14], $LnBaCo_2O_{5+\delta}$ (Ln = Pr, Gd) (PBC or GBC) [15,16], $La_2NiO_{4+\delta}$ [17], etc.

Being an important magnetoelectric basic component, $BaFeO_{3-\delta}$-based perovskites are extensively used as photocatalyst, NO_x absorber, oxygen-permeable membrane, and oxygen reduction electrocatalyst with a large variety of properties [18–21]. As for A-site cations, Ba^{2+} is a desirable candidate since the low oxidation state and large ionic size could facilitate the formation of oxygen vacancies by charge compensation and enlarge the free volume in the perovskite lattice, thus promoting oxygen ion mobility [22]. With regard to B-site metals, iron ions present some attractive properties such as abundant availability, high chemical stability associated with the less flexible redox behavior relative to cobalt ions and favorable electrocatalytic activity for ORR, enabling it to be an essential constituent [23]. However, $BaFeO_{3-\delta}$ adopts various crystal structures depending on the oxygen deficiency, including triclinic, rhombohedral, tetragonal and hexagonal structures, which are sensitive to the synthesis conditions (e.g., temperature, atmosphere and pressure) [24,25]. Additionally, $BaFeO_{3-\delta}$ parent material still possesses a multiphase structure within the temperature range of cell operation [21]. Consequently, doping strategy by substituting proper cations into $BaFeO_{3-\delta}$ is widely applied to stabilize a single perovskite lattice structure and tailor the properties of oxides [26–36].

In contrast to A-site substitution, B-site substitution leads to charge redistribution and geometric restructuring throughout the crystal lattice, which may be responsible for the lower energy cost for oxygen vacancy formation relative to A-site substitution [36]. It is generally acceptable that the B-site cations are mainly responsible for the electrocatalytic activity of perovskite oxides. Therefore, many attempts have been made to tune the electrochemical properties by proper selection of the B-site dopants [29–34]. Among them, Sn^{4+} was found to be an advisable dopant to stabilize the lattice structure of parent oxides in view of the following factors [37]: (1) wide availability with relatively low cost; (2) larger ionic radius over iron ions to diminish the difference in size between A-site and B-site cations; (3) stable oxidation state against thermal reduction; (4) higher metal-oxygen bond energy in comparison with Fe-O. Additionally, considering the higher valence state (+4) of tin relative to iron ions, the minor doping amount into the lattice structure is preferred to maintain favorable oxygen vacancies as the charge carriers.

The aim of the present work is to stabilize a single perovskite phase structure of $BaFeO_{3-\delta}$ parent oxide by doping a minor amount of Sn^{4+} into B-site, with desirable electrocatalytic properties as a cathode material in intermediate-temperature SOFCs (IT-SOFCs). The properties of the new perovskite of $BaFe_{0.95}Sn_{0.05}O_{3-\delta}$ (BFS) within the temperature range of cell operation are characterized by in-situ X-ray diffraction, scanning transmission electron microscope, thermal analysis, electrical transport, and electrochemical performance measurements.

2. Experimental

2.1. Powder synthesis

The BFS powder was prepared by a solid state process. Stoichiometric amounts of $BaCO_3$, Fe_2O_3 and SnO_2 as the cation sources were weighed, and then mixed in a ball milling (Fritsch, Pulverisette 6) using ethanol as a solvent medium at a rotational speed of 400 rpm for 1 h. The slurry mixture was dried, followed by calcination at 1000 °C for 10 h in air. The grinding and further calcination (at 1200 °C for 10 h) steps were repeated to form the final perovskite oxide.

2.2. Cell fabrication

To make BFS|SDC|BFS symmetrical cells, SDC pellets were prepared through uniaxial pressing, followed by sintering at 1400 °C for 5 h to obtain a dense electrolyte membrane. The BFS slurry was fabricated by mixing the cathode powder with glycerol, ethylene glycol, and isopropyl alcohol by ball-milling at 400 rpm for 0.5 h. The resulting colloidal suspension was sprayed symmetrically onto both surfaces of the SDC pellet and subsequently fired at 1000 °C in air for 2 h. Silver paste was then deposited as the current collector for the electrodes.

A complete single fuel cell with the configuration of NiO + YSZ|YSZ|SDC|BFS was constructed for the performance test. The NiO + YSZ anode substrate was first tape-cast, laminated and pre-fired at 1100 °C. Then, a YSZ electrolyte layer and a SDC buffer layer were in sequence deposited on the anode support through the wet powder spraying followed by sintering at 1400 °C for 5 h and 1350 °C for 5 h in air, respectively. The BFS cathode slurry was then applied to the SDC surface using the same procedures as described before for the fabrication of symmetrical cells.

2.3. Electrochemical test

The area specific resistances (ASR) of BFS electrode on the symmetrical cells were measured with the electrochemical impedance spectroscopy (EIS) using a Solartron 1287 potentiostat and a Solartron 1260 frequency response analyzer over the temperature range of 550–750 °C. Impedance spectra were acquired under open circuit voltage (OCV) conditions in a frequency range from 0.1 MHz to 0.1 Hz with an AC amplitude of 10 mV.

For fuel cell performance tests, the button cell was sealed onto a quartz tube with silver paste, placed inside a furnace and heated to the desired temperature. The cathode was exposed to ambient air, while the anode was fueled with pure hydrogen at a flow rate of 80 mL min^{-1}. The current-voltage (I-V) polarization curves were recorded with a Keithley 2420 source meter using a four-probe configuration between 550 and 750 °C.

2.4. Material characterization

An in-situ X-ray diffractometer (XRD, Philips X'Pert Pro, Cu Kα radiation) was employed to confirm the crystalline structures of sample. The diffraction patterns were collected in a scanning range of 20–80° with a step size of 0.02° across the temperature range from room temperature to 800 °C. The experimental data were refined using the Rietveld method with the General Structure

Analysis System (GSAS) program. Scanning transmission electron microscope (STEM, JEOL JEM-2100F) equipped with energy-dispersive X-ray (EDX) was used to observe the crystallographic morphology and chemical composition of the specimen.

The initial oxygen non-stoichiometry at room temperature was determined by iodometric titration method, as described elsewhere [27]. Moreover, the oxygen content at elevated temperatures was examined by the thermo-gravimetric analysis (TGA, NETZSCH, STA 449 F3) from room temperature to 800 °C at a heating rate of 10 °C min^{-1} in air.

The cathode powder was compressed and sintered to obtain dense bar-shaped specimens with the geometric dimensions of 2 mm × 5 mm × 12 mm for conductivity testing, which was performed using a four-probe DC method with a Keithley 2420 source meter. The electrical conductivity measurement was conducted over a temperature range of 500–800 °C at intervals of 10 °C under oxygen partial pressures of 0.21 and 0.1 atm. The oxygen kinetics, e.g., surface exchange and bulk diffusion, was analyzed by the electrical conductivity relaxation (ECR) technique. After conductivity reached an equilibrium state, the oxygen activity was abruptly changed from 0.21 to 0.1 atm, leading to a variation of oxygen vacancy concentration in the specimens. The corresponding change in conductivity was detected continuously as a function of the time.

3. Results and discussion

3.1. Structural analysis

Fig. 1 displays the XRD pattern of BFS powder at room temperature. It could be realized that the diffraction profile fails to be assigned to a single pure phase; therefore, multiple phases need to be adopted for BFS oxide at room temperature. Although Sn^{4+} doping still fails to stabilize the single phase of BFS down to room temperature, the phase structure of perovskite materials within the intermediate-temperature range between 500 and 800 °C deserves to be investigated since it is the operating temperatures of electrode materials. In order to examine possible phase transition behavior with an increase in temperature, in-situ high-temperature XRD was performed in air within a temperature range of 100–800 °C at an interval of 100 °C and the results are exhibited in Fig. 2a and b. It can be seen that as the temperature increases, the profile of two split peaks, belonging to the main characteristic peaks of sample, reduces by degrees and then merges into a singlet at around 500 °C, corresponding to the multiple-to-single phase transition. This transition is likely driven by the thermal reduction of iron ions at approximately 500 °C, which results in tending to be octahedral [FeO_6] for B-site, thereby improving the symmetry of the BFS lattice structure [33,38]. Afterwards, this single phase structure can be retained upon further heating till 800 °C, indicating the thermodynamically stable state within the temperature range of cell operation. Taking BFS at 700 °C as an example, as shown in Fig. 2c, based on Rietveld refinement, the in-situ XRD patterns can be readily assigned to a cubic symmetrical perovskite structure with unit cell data, a = b = c = 4.101(1) Å. It fits well using the *Pm*-3*m* structural model with the low reliability factors of R_{wp} = 6.62%, R_p = 6.03% and Chi^2 = 1.317, confirming the validity of this model. Therefore, BFS actually adopts the cubic perovskite structure with the space group *Pm*-3*m* under the fuel cell operating conditions despite the observed multiple phases at room temperature.

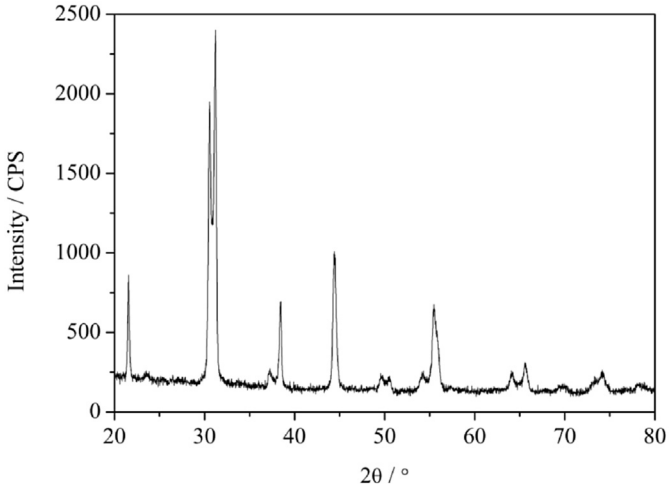

Fig. 1. XRD pattern of BFS powder synthesized by a solid-state reaction route at 1200 °C for 10 h.

Further evidence of the cubic perovskite structure at elevated temperatures came from STEM technique. Fig. 3a depicts the large field-of-view high-resolution STEM image of BFS sample quenched at 700 °C. The well-defined lattice fringes with an inter-planar interval of 0.291 nm in the magnified view of the selected region (Fig. 3b) can be indexed into (1 1 0) plane of the cubic structure with the space group *Pm*-3*m*, in good consistence with the in-situ XRD analysis. This is further confirmed by the corresponding fast Fourier transform (FFT) patterns along the [1$\bar{1}$0] zone axis, with the relevant lattice planes (1 1 0) and (1 1 1) marked in Fig. 3c. EDX diffraction spectrum, taken in the STEM from the BFS specimen quenched at 700 °C as shown in the Supplementary Materials (Fig. S1), reveals the incorporation of tin into the BFS phase by the presence of tin signal. The relative abundances of the cations are in accordance with the expected stoichiometry (nominal molar ratios).

3.2. Oxygen non-stoichiometry

It is generally believed that the high oxygen vacancy concentration within the temperature range of cell operation can improve the electrocatalytic activity of cathode materials, since the oxygen vacancies provide active sites for surface diffusion process and charge transfer process of non-charged or charged oxygen species [39]. The temperature dependences of oxygen non-stoichiometry and average valence state of iron ions were investigated by combining TGA data and initial oxygen non-stoichiometry value determined by iodometric titration with the results being presented in Fig. 4. The intermediate temperature range matches approximately the one employed for the electrochemical evaluation of cathode. It is clear to see that the oxygen vacancy concentration increases continuously with increasing temperature, compensated by the decrease in oxidation state of iron ions due to the thermal reduction. At the cell operating temperatures, high oxygen non-stoichiometry values (e.g., δ = 0.443 at 700 °C) are obtained, a desirable property for ORR activity of cathode materials.

3.3. Transport properties

In general, the cathode may be subjected to relatively lower oxygen partial pressures due to cathodic polarization under fuel cell operating conditions. The dependences of electrical conductivity of BFS on the temperature (500–800 °C) and oxygen partial pressure (PO_2 = 0.21 and 0.1 atm) are displayed in Fig. 5. At a given temperature, the electrical conductivity increases with increasing PO_2, indicating a p-type electron hole conduction mechanism, which is also supported by the average oxidation state higher than

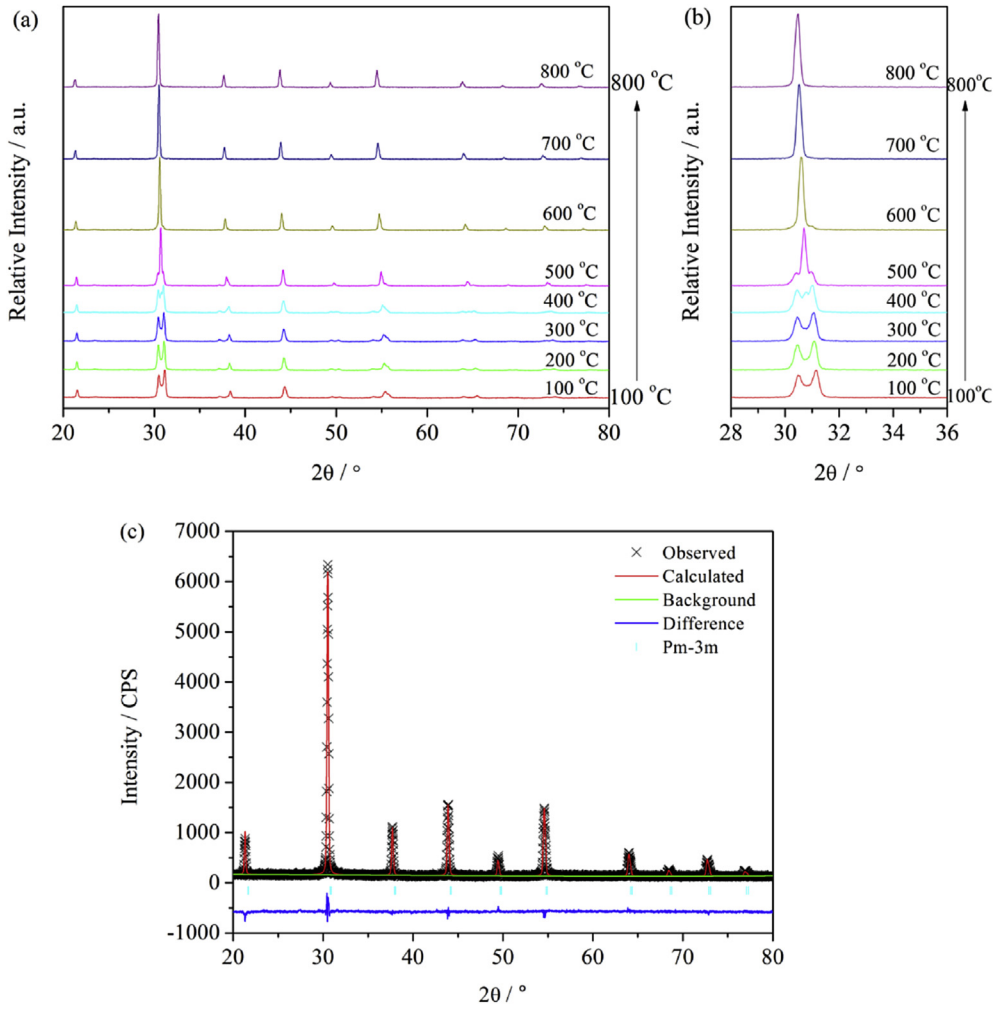

Fig. 2. (a) In-situ XRD patterns of BFS over the temperature range between 100 and 800 °C in air; (b) magnified in-situ XRD patterns from 28 to 36°; (c) Rietveld refinement plot of an example BFS at 700 °C for in-situ XRD pattern.

3 + of iron ions as shown in Fig. 4. In addition, the electrical conductivity of BFS sample decreases continuously with increasing temperature, exhibiting a metallic conducting behavior, analogous to that of previously studied B-site doped $BaFeO_{3-\delta}$ [32,40]. This may be because the high temperature facilitates the thermal reduction of iron ions, accompanied by the formation of oxygen vacancies, which results in the decrease of electron holes as the charge carriers and disturbance of the (Fe, Sn)-*O*-(Fe, Sn) periodic potential [41]. It can be also expressed using the following Kröger-Vink notation [42].

$$2Fe_{Fe}^{\cdot} + O_O^{\times} \leftrightarrow 2Fe_{Fe}^{\times} + V_O^{\cdot\cdot} + 1/2O_2 \quad (1)$$

It is generally accepted that ORR catalytic activity of cathode is considerably related to the intrinsic properties of materials, e.g., oxygen bulk diffusion and surface exchange properties (D_{chem} and K_{chem} values). These parameters were obtained using the ECR technique on the basis of the change in surrounding atmosphere. The sudden variation in oxygen partial pressure (PO_2) of the ambient atmosphere leads to a corresponding change in the charge carrier (oxygen vacancy) concentration as a result of the local electroneutrality requirement [43]. The ECR process is accompanied by oxygen exchange on the surface and chemical diffusion in the bulk of the sample, which can be fitted to the relevant equations previously reported elsewhere with MATLAB [44]. After an abrupt change in PO_2 from 0.21 to 0.1 atm at 700 °C, the typical ECR profile for BFS is shown in Fig. 6. The relaxation process experiences a short time to reach a new equilibrium, suggesting a quick response to the change in PO_2. High D_{chem} and K_{chem} values of 1.86×10^{-4} cm^2 s^{-1} and 1.92×10^{-3} cm s^{-1} for BFS are achieved at 700 °C, which are comparable to those of previously investigated $BaFeO_{3-\delta}$-derived materials [35,45]. The high oxygen vacancy concentration and large lattice size of the single cubic phase structure for Sn-doped $BaFeO_{3-\delta}$ are beneficial to the mobility of oxygen species, thus contributing to fast oxygen surface exchange and bulk diffusion.

3.4. Electrochemical evaluation

The area specific resistance (ASR) of BFS was evaluated in a symmetrical configuration using AC impedance spectroscopy under OCV conditions, and the representative Nyquist plot at 700 °C is shown in Fig. 7a. The ASR (R_p) value is determined by the intercept between high- and low-frequency on the real axis of the Nyquist plot. The relatively lower ASR value of 0.033 Ω cm^2, originating from the single cubic perovskite structure and fast oxygen kinetics, is obtained for BFS at 700 °C, compared with that of previously studied related cathode materials [46,47]. Additionally, the exchange current density i_0, a direct reflection of intrinsic electrocatalytic activity, can be obtained from the EIS measurement. The i_0

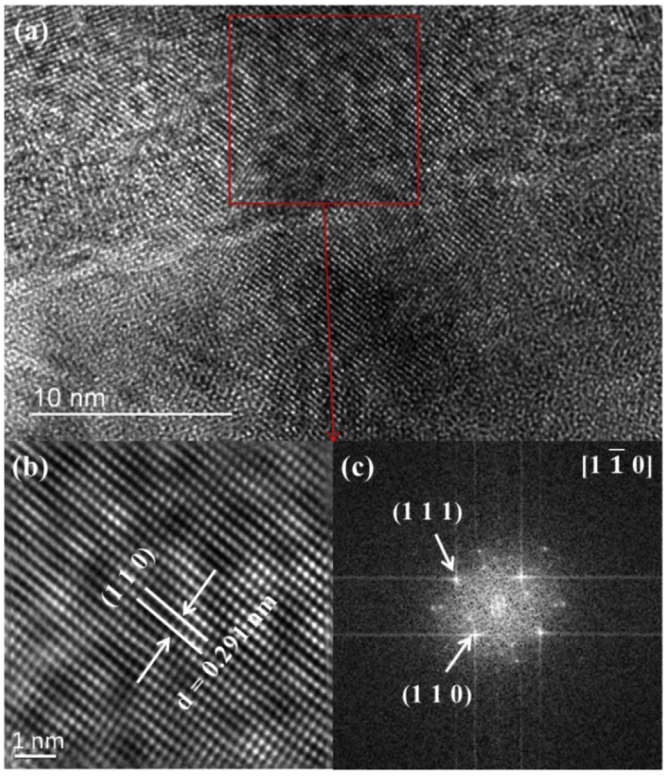

Fig. 3. (a) A high-resolution STEM image of BFS sample quenched at 700 °C; (b) the corresponding magnified view showing lattice fringes and (c) FFT patterns of the selected region.

value is measured from R_p of the Nyquist plot and calculated using Eq. (2), which is derived from the low-field approximation to Bulter-Volmer equation [48]:

$$i_0 = RTv/nFR_p \quad (2)$$

where R, T and F have their usual meanings, v is the number of times that the rate-determining step occurs for one occurrence of the full reaction, and n is the total number of electrons passed in the reaction. For the ORR mechanism, the ratio of v/n is considered as 1/4 under the current experimental conditions. The i_0 value for BFS

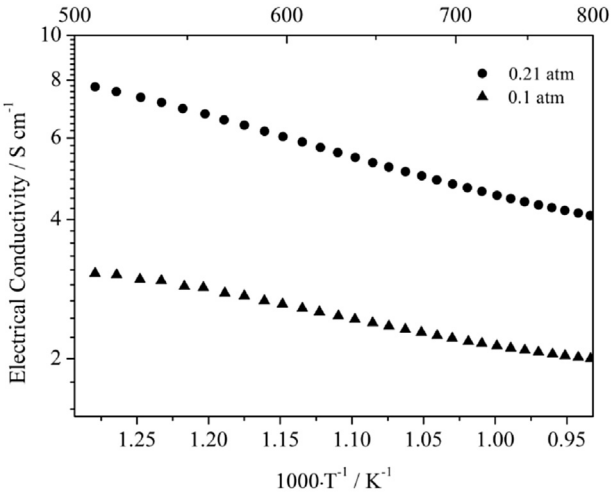

Fig. 5. Electrical conductivity of BFS in 21% and 10% oxygen as a function of temperature.

cathode is 635.3 mA cm^{-2} at 700 °C. Fig. 7a also exhibits the Arrhenius format of the ASR values as a function of the reciprocal of absolute temperature at temperatures ranging from 550 to 750 °C. The good linearity of the Arrhenius plot indicates the stable structure of BFS cathode within the investigated temperature range. The overall activation energy for ORR obtained from the slope of the Arrhenius plot is determined to be ~124 kJ mol^{-1} for BFS cathode.

The durability of cathode materials is a critical factor for the practical applications of IT-SOFCs. The long-term stability of BFS cathode was investigated based on the symmetrical configuration of BFS|SDC|BFS under OCV conditions. As shown in Fig. 7b, the ASR value of BFS cathode is recorded as a function of operation time at 700 °C. Over the 300 h long-term testing period, although a slight fluctuation is observed, the ASR value remains relatively stable at around 0.03 Ω cm^2, demonstrating the high potential of BFS as a cathode material for IT-SOFCs.

With BFS as cathode, the electrochemical performance was evaluated between 550 and 750 °C in a single cell configuration with NiO + YSZ served as anode, YSZ layer as supporting electrolyte and SDC layer as buffer interlayer, and the corresponding results are presented in Fig. 8. The OCV value is 1.07 V at 700 °C, which comes

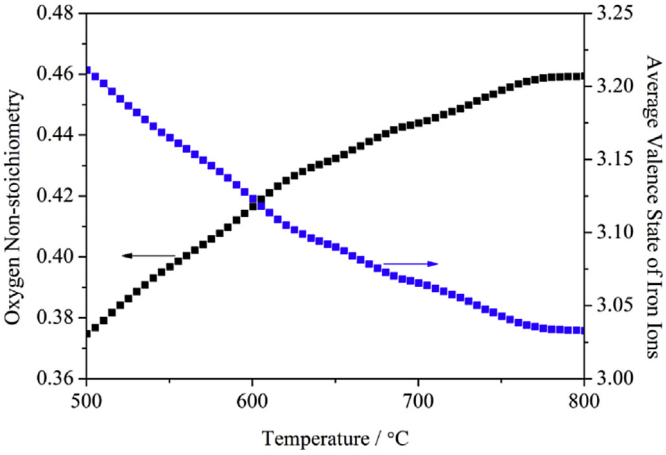

Fig. 4. Thermo-gravimetric data of BFS presenting a variation of oxygen non-stoichiometry and average valence state of iron ions with temperature.

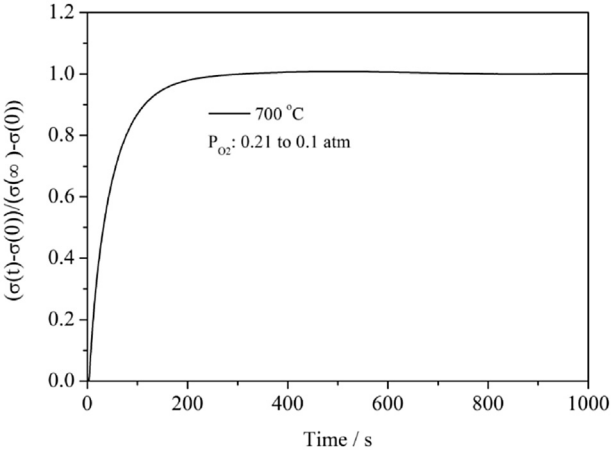

Fig. 6. ECR response of BFS at 700 °C after an abrupt change of oxygen partial pressure from 0.21 to 0.1 atm.

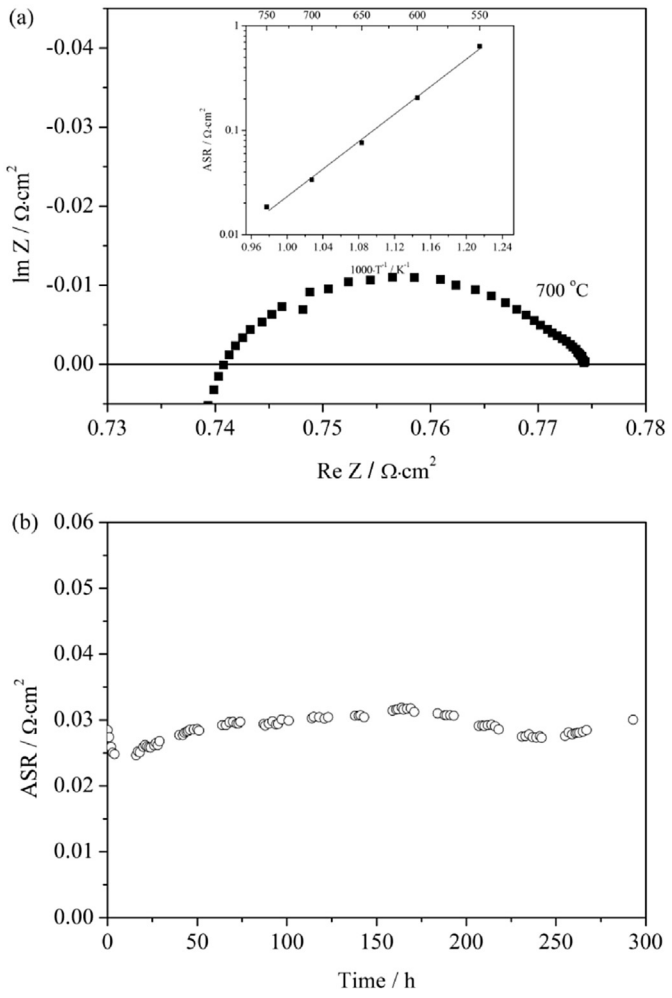

Fig. 7. (a) Typical Nyquist impedance spectrum of BFS at 700 °C in air and Arrhenius plot of the ASR values at various temperatures shown as an inset; (b) time dependence of the polarization resistance for BFS cathode at 700 °C under OCV conditions.

near to the theoretical one, indicating a dense electrolyte and the good sealing. With air as oxygen source and hydrogen as fuel, the cell yields a peak power density of 1033 mW cm^{-2} at 700 °C, which

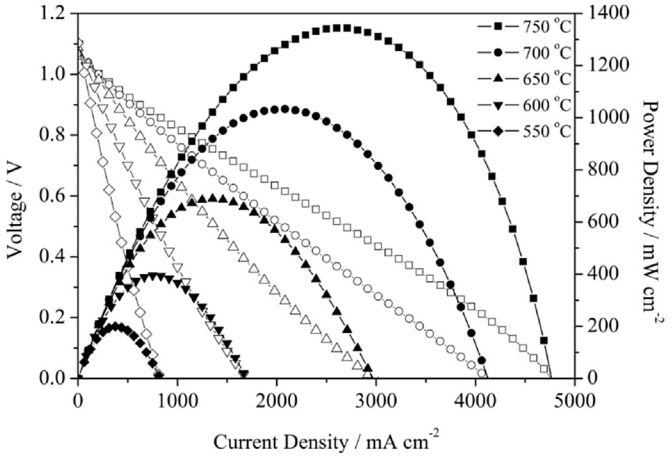

Fig. 8. I-V polarization curves and corresponding power density curves of single cell for BFS cathode at various temperatures.

is higher than that of similar cells by applying other cobalt-free ferrite-based cathode materials [49,50]. The favorable electrocatalytic activity is believed to be consistent with the sustained single cubic perovskite structure and high oxygen vacancy concentration under the fuel cell operating conditions, suggesting a promising candidate of BFS oxide as an oxygen reduction electrocatalyst for IT-SOFCs.

4. Conclusions

With an aim to stabilize the crystal structures of $BaFeO_{3-\delta}$ parent oxide, a B-site tin-doped perovskite oxide $BaFe_{0.95}Sn_{0.05}O_{3-\delta}$ (BFS) was fabricated and investigated, with a focus on lattice structure, oxygen vacancy concentration, electrical conductivity, oxygen bulk diffusion and surface exchange, and electrochemical performance. BFS oxide maintains a single cubic symmetrical structure in the *Pm*-3*m* space group under the fuel cell operating conditions in despite of the observed multiple phases at room temperature. The BFS-derived cells exhibit superior electrocatalytic activities, e.g., low polarization resistance of 0.033 Ω cm^2 and high peak power density of 1033 mW cm^{-2} at 700 °C. The high activity for ORR of BFS cathode may be attributed to its fast oxygen bulk diffusion and surface exchange properties, which could be rationalized by the sustained single cubic symmetrical structure and high oxygen vacancy concentration over the temperature range of cell operation. The desirable electrochemical activity and long-term stability of BFS oxide warrant it further study and optimization as a promising cathode material for IT-SOFCs.

Acknowledgements

This work was supported by a grant from Research Grant Council, University Grants Committee, Hong Kong SAR (PolyU 5326/12E).

Appendix A. Supplementary data

Supplementary data related to this article can be found at http://dx.doi.org/10.1016/j.jpowsour.2016.07.023.

References

[1] A.B. Stambouli, E. Traversa, Renew. Sustain. Energy Rev. 6 (2002) 433–455.
[2] A.J. Jacobson, Chem. Mater. 22 (2010) 660–674.
[3] E.D. Wachsman, C.A. Marlowe, K.T. Lee, Energy Environ. Sci. 5 (2012) 5498–5509.
[4] D.J.L. Brett, A. Atkinson, N.P. Brandon, S.J. Skinner, Chem. Soc. Rev. 37 (2008) 1568–1578.
[5] Y. Chen, W. Zhou, D. Ding, M. Liu, F. Ciucci, M. Tade, Z. Shao, Adv. Energy Mater. 5 (2015), 1500537:1–34.
[6] M.J. Jørgensen, M. Mogensen, J. Electrochem. Soc. 148 (2001) A433–A442.
[7] S.P. Jiang, J. Mater. Sci. 43 (2008) 6799–6833.
[8] H. Fukunaga, M. Koyama, N. Takahashi, C. Wen, K. Yamada, Solid State Ionics 132 (2000) 279–285.
[9] C. Xia, W. Rauch, F. Chen, M. Liu, Solid State Ionics 149 (2002) 11–19.
[10] E.P. Murray, M.J. Sever, S.A. Barnett, Solid State Ionics 148 (2002) 27–34.
[11] F. Tietz, V.A.C. Haanappel, A. Mai, J. Mertens, D. Stöver, J. Power Sources 156 (2006) 20–22.
[12] Z. Shao, S.M. Haile, Nature 431 (2004) 170–173.
[13] Q.L. Liu, K.A. Khor, S.H. Chan, J. Power Sources 161 (2006) 123–128.
[14] H. Orui, K. Watanabe, R. Chiba, M. Arakawa, J. Electrochem. Soc. 151 (2004) A1412–A1417.
[15] G. Kim, S. Wang, A.J. Jacobson, L. Reimus, P. Brodersen, C.A. Mims, J. Mater. Chem. 17 (2007) 2500–2505.
[16] F. Dong, M. Ni, Y. Chen, D. Chen, M.O. Tade, Z. Shao, J. Mater. Chem. A 2 (2014) 20520–20529.
[17] S.J. Skinner, J.A. Kilner, Solid State Ionics 135 (2000) 709–712.
[18] Y. Yang, Y. Jiang, Y. Wang, Y. Sun, J. Mol. Catal. A Chem. 270 (2007) 56–60.
[19] H. Xian, X. Zhang, X. Li, L. Li, H. Zou, M. Meng, Q. Li, Y. Tan, N. Tsubaki, J. Phys. Chem. C 114 (2010) 11844–11852.
[20] K. Watenabe, M. Yuasa, T. Kida, Y. Teraoka, N. Yamazoe, K. Shimanoe, Adv. Mater. 22 (2010) 2367–2370.

[21] F. Dong, Y. Chen, D. Chen, Z. Shao, ACS Appl. Mater. Interfaces 6 (2014) 11180–11189.
[22] B. Qian, Y. Chen, M.O. Tade, Z. Shao, J. Mater. Chem. A 2 (2014) 15078–15086.
[23] G. Yang, C. Su, Y. Chen, F. Dong, M.O. Tade, Z. Shao, J. Eur. Ceram. Soc. 35 (2015) 2531–2539.
[24] S. Mori, J. Am. Ceram. Soc. 49 (1966) 600–605.
[25] J.M. Gonzalez-calbet, M. Parras, M. Vallet-regi, J.C. Grenier, J. Solid State Chem. 86 (1990) 149–159.
[26] T. Kida, D. Takauchi, K. Watanabe, M. Yuasa, K. Shimanoe, Y. Teraoka, N. Yamazoe, J. Electrochem. Soc. 156 (2009) E187–E191.
[27] F. Dong, D. Chen, Y. Chen, Q. Zhao, Z. Shao, J. Mater. Chem. 22 (2012) 15071–15079.
[28] W.D. Penwell, J.B. Giorgi, Sens. Actuators B 191 (2014) 171–177.
[29] X. Zhu, H. Wang, W. Yang, Solid State Ionics 177 (2006) 2917–2921.
[30] K. Watanabe, D. Takauchi, M. Yuasa, T. Kida, K. Shimanoe, Y. Teraoka, N. Yamazoe, J. Electrochem. Soc. 156 (2009) E81–E85.
[31] T. Kida, A. Yamasaki, K. Watanabe, N. Yamazoe, K. Shimanoe, J. Solid State Chem. 183 (2010) 2426–2431.
[32] X. Liu, H. Zhao, J. Yang, Y. Li, T. Chen, X. Lu, W. Ding, F. Li, J. Membr. Sci. 383 (2011) 235–240.
[33] F. Dong, Y. Chen, R. Ran, D. Chen, M.O. Tade, S. Liu, Z. Shao, J. Mater. Chem. A 1 (2013) 9781–9791.
[34] Y. Lu, H. Zhao, X. Cheng, Y. Jia, X. Du, M. Fang, Z. Du, K. Zheng, K. Swierczek, J. Mater. Chem. A 3 (2015) 6202–6214.
[35] J. Wang, M. Saccoccio, D. Chen, Y. Gao, C. Chen, F. Ciucci, J. Power Sources 297 (2015) 511–518.
[36] Z.M. Baiyee, C. Chen, F. Ciucci, Phys. Chem. Chem. Phys. 17 (2015) 23511–23520.
[37] Z. Zhang, Y. Chen, M.O. Tade, Y. Hao, S. Liu, Z. Shao, J. Mater. Chem. A 2 (2014) 9666–9674.
[38] S. Jiang, W. Zhou, Y. Niu, Z. Zhu, Z. Shao, ChemSusChem 5 (2012) 2023–2031.
[39] S.B. Adler, Chem. Rev. 104 (2004) 4791–4843.
[40] M. Zhu, Z. Cai, T. Xia, Q. Li, L. Huo, H. Zhao, Int. J. Hydrogen Energy 41 (2016) 4784–4791.
[41] K.T. Lee, A. Manthiram, Chem. Mater. 18 (2006) 1621–1626.
[42] F.A. Kröger, H.J. Vink, Solid State Phys. 3 (1956) 307–435.
[43] J.E.T. Elshof, M.H.R. Lankhorst, H.J.M. Bouwmeester, J. Electrochem. Soc. 144 (1997) 1060–1067.
[44] D. Chen, Z. Shao, Int. J. Hydrogen Energy 36 (2011) 6948–6956.
[45] D. Xu, F. Dong, Y. Chen, B. Zhao, S. Liu, M.O. Tade, Z. Shao, J. Membr. Sci. 455 (2014) 75–82.
[46] C. Chen, D. Chen, Y. Gao, Z. Shao, F. Ciucci, J. Mater. Chem. A 2 (2014) 14154–14163.
[47] X. Ding, X. Gao, W. Zhu, J. Wang, J. Jiang, Int. J. Hydrogen Energy 39 (2014) 12092–12100.
[48] J. Liu, A.C. Co, S. Paulson, V.I. Birss, Solid State Ionics 177 (2006) 377–387.
[49] J. Yin, Y. Yin, J. Lu, C. Zhang, N.Q. Minh, Z. Ma, J. Phys. Chem. C 118 (2014) 13357–13368.
[50] Y. Bu, D. Ding, S.Y. Lai, D. Chen, X. Xiong, T. Wei, Q. Zhong, J. Power Sources 275 (2015) 808–814.